

Arbitrary Beam Pattern Approximation via RISs with Measured Element Responses

Moustafa Rahal^{*‡}, Benoît Denis^{*}, Kamran Keykhosravi[†],
Musa Furkan Keskin[†], Bernard Uguen[‡], George C. Alexandropoulos[§], and Henk Wymeersch[†]

^{*}CEA-Leti, Université Grenoble Alpes, F-38000 Grenoble, France

[†]Department of Electrical Engineering, Chalmers University of Technology, Gothenburg, Sweden

[‡]Université Rennes 1, IETR - UMR 6164, F-35000 Rennes, France

[§]Department of Informatics and Telecommunications, National and Kapodistrian University of Athens, Greece

Abstract—Smart radio environments (SREs) are seen as a key rising concept of next generation wireless networks, where propagation channels between transmitters and receivers are purposely controlled. One promising approach to achieve such channel flexibility relies on semi-passive reflective Reconfigurable intelligent surfaces (RISs), which can shape the bouncing multipath signals for enhancing communication quality of service, making localization feasible in adverse operating conditions, or reducing unwanted electromagnetic emissions. This paper introduces a generic framework that aims at optimizing the end-to-end precoder controlled by RISs, so that arbitrary beam patterns can be generated, given a predefined lookup table of RIS element-wise complex reflection coefficients. This method is validated and illustrated for different targeted beam patterns in both the far-field and the near-field regimes, while considering the prior characterization of real-life RIS hardware prototypes. These results show how, and to which extent, RIS configuration optimization can approximate the desired beams under realistic hardware limitations and low-complexity implementation practicability, or conversely, which RIS elements' lookup tables would be more suitable. The latter can provide useful guidelines for future RIS hardware designs.

Index Terms—Reconfigurable intelligent surface, reflective beamforming, optimization, lookup table, reflection coefficients, smart radio environments.

I. INTRODUCTION

Reconfigurable intelligent surfaces (RISs) are envisioned as an important enabling technology for beyond fifth generation (5G) wireless systems [1], [2]. They have several attractive properties that allow them to boost performance, without requiring installing and maintaining expensive base station (BS) infrastructure. While originally envisioned as a means to overcome line-of-sight (LoS) blockage and extend radio coverage, they have proven to be a versatile tool to control the wireless propagation environment, with applications to localization, radar and radio mapping, security, energy efficiency, and reduced electromagnetic field exposure [3], [4].

An important property of RISs is that they are largely passive, requiring only per-element control to modify and redirect externally generated radio signals [5]. To further reduce cost, RISs may be made of low-cost hardware, and thus suffer more from imperfections than standard infrastructure [6], [7]. The optimization of the RIS unit elements can be targeted to steer reflected energy towards desired users as well as to optimize localization and sensing performance, similar to phased arrays

[8]. There are several models for the RIS element control, including pure phase control [1], quantized phase control [9], amplitude-dependent phase control [10], and joint amplitude and phase control [11], which all require tailored optimization. A unified way of treating all such models is through a lookup table, listing all possible pairs of amplitude and phase that may be realizable at each element with a given RIS hardware. Such a table can also account for coupling effects, which are challenging to treat analytically.

The optimization of RIS configuration (based on lookup tables or more conventional descriptions) can be approached in two ways: *i*) directly optimizing the RIS configuration based on the considered objective (e.g., maximize rate or received signal strength, or minimize the position error bound) [1], [2], [10], [12]; and *ii*) performing first an unconstrained optimization of the RIS configuration and then finding the best approximation that can be supported by the RIS. We can call these approaches *constrain, then optimize* or *optimize, then constrain*. For the second approach, suitable methods should be developed that best match the unconstrained beam pattern.

Optimization of RIS configuration can be more broadly interpreted as a constrained beam design problem, which has been extensively studied for phased arrays, in both communication and radar literature. For instance, the so-called *multibeam*s were proposed in [13] to support joint communication and sensing, while in [14], the so-called derivative (i.e., *difference*) beams from the monopulse radar literature [15] were proposed to support accurate localization, and were later extended to an RIS setting in [16]. The main distinction between a reflective RIS and a phased array radar is that separate beamforming architectures are commonly employed in radar hardware to create azimuth- and elevation-difference beams in reception [17], [18], while a reflective RIS does not produce receive beams via dedicated hardware, and can only passively reflect the impinging signals through optimized phase control. Hence, it is worth investigating how RIS phase profiles can be designed under lookup table constraints to produce *difference* beams. Such beams are two examples of non-standard beams that differ from traditional directional beams (steering vectors). An important challenge with constraining optimized beams is that constraints may be difficult to handle analytically, e.g., unit-norm constraints are non-

convex and require iterative methods [19]. In some cases, the RIS element configurations are quantized [20], exhibit phase-dependent amplitude variations [10], or are only described through a lookup table based on measurements [21].

In this paper, we present a computationally efficient method to optimize the configurations of reflective RISs from an arbitrary lookup table (including RIS element responses based on measurements), in order to approximate arbitrary complex beam patterns. The proposed approach can account for both far-field and near-field effects, and is amenable to a low-complexity implementation. We demonstrate the proposed approach for several beam types (directional beam, multi-beam, and derivative beam) and several lookup tables, derived from the experimental characterization of real RISs.

Notations: Vectors and matrices are, respectively, denoted by lower-case and upper-case bold letters (e.g., \mathbf{x} , \mathbf{X}). The notation $[\mathbf{a}]_i$ is used to point at the i -th element of vector \mathbf{a} , and similarly, $[\mathbf{A}]_{i,j}$ represents the element in the i -th row and j -th column of matrix \mathbf{A} , while $i:j$ is used to specify all the elements between indices i and j . The Hadamard product is denoted by \odot and $\dot{\mathbf{a}}_x = \partial \mathbf{a} / \partial x$ is the partial derivation of \mathbf{a} with respect to (w.r.t.) x . Moreover, the notations $(\cdot)^\top$, $(\cdot)^*$ and $(\cdot)^H$ denote the matrix transposition, conjugation, and Hermitian conjugation, respectively. Finally, $(\cdot)^{(r)}$ denotes the r -th iteration in a loop and $\text{proj}_{\mathcal{V}}(\mathbf{x})$ represents the projection of vector \mathbf{x} onto the set \mathcal{V} .

II. SYSTEM MODEL AND PROBLEM FORMULATION

In this section, we describe the RIS-enabled wireless communication system under investigation, together with the considered design problem formulation for RIS-based arbitrary complex beam patterns.

A. System Model

We consider a wireless system comprising a single-antenna transmitter (TX) wishing to communicate with a single-antenna receiver (RX) in a scenario where the LoS link is blocked, similar to [22]. Their communication is assumed to be enabled by an M -element reflective RIS, whose placement results in two LoS links: one between the TX and the RIS, and the other between the RIS and the RX. By considering narrowband transmissions, the baseband received signal can be mathematically expressed as follows [16], [23]:

$$\begin{aligned} y &= \alpha \mathbf{a}^\top(\mathbf{p}_{\text{RX}}) \mathbf{\Omega} \mathbf{a}(\mathbf{p}_{\text{TX}}) x + n \\ &= \alpha \omega^\top \mathbf{b}(\mathbf{p}_{\text{RX}}, \mathbf{p}_{\text{TX}}) x + n, \end{aligned} \quad (1)$$

where \mathbf{p}_{TX} and \mathbf{p}_{RX} are, respectively, the TX and RX position points, α denotes the complex channel gain, $\mathbf{\Omega} \triangleq \text{diag}(\boldsymbol{\omega})$ with the M -element column vector $\boldsymbol{\omega}$ including the RIS complex configuration, x is the transmitted signal with energy E_s , $n \sim \mathcal{CN}(0, N_0)$ represents the additive white Gaussian noise of power spectral density N_0 , and the M -element column vector $\mathbf{a}(\cdot)$ is the response of the RIS panel. Considering a point \mathbf{p} placed at either a far-field distance or a near-field distance from the RIS, the m -th ($m = 1, 2, \dots, M$) entry of $\mathbf{a}(\mathbf{p})$, with

respect to the m -th RIS element \mathbf{p}_m and the RIS phase center \mathbf{p}_{RIS} , is given by¹

$$[\mathbf{a}(\mathbf{p})]_m = \exp\left(-j \frac{2\pi}{\lambda} (\|\mathbf{p} - \mathbf{p}_m\| - \|\mathbf{p} - \mathbf{p}_{\text{RIS}}\|)\right), \quad (2)$$

where λ is the wavelength. Finally, in (1), we have used the definition $\mathbf{b}(\mathbf{p}_{\text{RX}}, \mathbf{p}_{\text{TX}}) \triangleq \mathbf{a}(\mathbf{p}_{\text{RX}}) \odot \mathbf{a}(\mathbf{p}_{\text{TX}})$.

B. Problem Formulation

Due to various hardware constraints [9], the tunable RIS reflection coefficients, which are modeled by the RIS configuration vector $\boldsymbol{\omega}$ in (1), do not take continuous values. Instead, for the m -th element of $\boldsymbol{\omega}$ holds $\omega_m \in \mathcal{V}$, where \mathcal{V} is usually a finite set of complex numbers with magnitude not exceeding unity. For example, according to the recent experimental characterization of individual RIS element responses, the set \mathcal{V} is given by [21, Table I]. Capitalizing on the model in (1) and given the practical constraints for $\boldsymbol{\omega}$, our goal in this paper is to devise a generic optimization framework for realizing any desired beam pattern via the reflective RIS, i.e.:

$$G(\mathbf{p}) = \boldsymbol{\omega}^\top \mathbf{b}(\mathbf{p}, \mathbf{p}_{\text{TX}}) \quad (3)$$

for any receiving point \mathbf{p} in a coverage area \mathcal{G} . Without loss of generality, \mathbf{p}_{RIS} and \mathbf{p}_{TX} are assumed fixed. Some examples of beam patterns, with $\mathbf{p}_{\text{des},j}$ ($j = 1, 2, \dots, J$) denoting any desired RX point(s) to steer a beam, are as follows:

- **Directional beams (including DFT beams):** In this case, it holds $G(\mathbf{p}) \propto (\mathbf{b}^*(\mathbf{p}_{\text{des},1}, \mathbf{p}_{\text{TX}}))^\top \mathbf{b}(\mathbf{p}, \mathbf{p}_{\text{TX}})$, where \propto indicates proportionality [23]; in this way, normalization issues can be avoided.
- **Derivative beams:** Derivative beams [24] correspond to difference beams used in monopulse radar [15], MIMO radar [25], or even localization [14]. For such beams, the beam pattern is $G(\mathbf{p}) \propto (\dot{\mathbf{b}}_x^*(\mathbf{p}_{\text{des},1}, \mathbf{p}_{\text{TX}}))^\top \mathbf{b}(\mathbf{p}, \mathbf{p}_{\text{TX}})$.
- **Multiple concurrent beams:** For the multi-beam case w.r.t. J desired RX points, the beam pattern becomes $G(\mathbf{p}) \propto (\sum_{j=1}^J \mathbf{b}^*(\mathbf{p}_{\text{des},j}, \mathbf{p}_{\text{TX}}))^\top \mathbf{b}(\mathbf{p}, \mathbf{p}_{\text{TX}})$.

III. METHODOLOGY

In this section, we present the design methodology for the configuration of reflective RISs that can lead to beam patterns as close as possible to predefined ones.

A. Least Squares Precoder Design

Building on [19], we discretize the desired beam pattern in (3) to create its N_G -element version \mathbf{g} , where each element of this vector corresponds to a distinct point in \mathcal{G} ; this implies that $[\mathbf{g}]_k = G(\mathbf{p}_k)$ with $k = 1, 2, \dots, N_G$. By constructing the $N_G \times M$ complex-valued matrix $\mathbf{B} \triangleq [\mathbf{b}^\top(\mathbf{p}_1, \mathbf{p}_{\text{TX}}); \dots; \mathbf{b}^\top(\mathbf{p}_{N_G}, \mathbf{p}_{\text{TX}})]$ and similar to [19, eq. (12)], we formulate the following optimization problem for the RIS configuration design:

$$\min_{\mathbf{s}, \boldsymbol{\omega}} \|\mathbf{g} - \mathbf{s} \mathbf{B} \boldsymbol{\omega}\|^2 \quad (4a)$$

$$\text{s.t. } \omega_m \in \mathcal{V}, m = 1, 2, \dots, M, \quad (4b)$$

¹Note that the model generalizes to the standard far-field model when the distance $\|\mathbf{p} - \mathbf{p}_{\text{RIS}}\|$ becomes large.

Algorithm 1 RIS Configuration Design

Initialize: $\beta \in (0, 1)$ and $\omega^{(0)} = \text{proj}_{\mathcal{V}}(\mathbf{B}^\dagger \mathbf{g})$.

- 1: **for** $r = 1, 2, \dots$ **do**
 - 2: Compute $s^{(r)} = \frac{(\omega^{(r-1)})^H \mathbf{B}^H \mathbf{g}}{\|\mathbf{B} \omega^{(r-1)}\|^2}$.
 - 3: Set $\omega_u^{(r)} = \omega^{(r-1)} + \frac{\beta \mathbf{B}^H (\mathbf{g} - s^{(r)} \mathbf{B} \omega^{(r-1)})}{\lambda_{\max}(|s^{(r)}|^2 \mathbf{B}^H \mathbf{B})}$.
 - 4: Calculate $\omega^{(r)} = \text{proj}_{\mathcal{V}}(\omega_u^{(r)})$ using Algorithm 2.
 - 5: **end for**
-

Algorithm 2 Projection onto set \mathcal{V} : $\omega_{\text{out}} = \text{proj}_{\mathcal{V}}(\omega_{\text{in}})$

- 1: **for** $m = 1, \dots, M$ **do**
 - 2: Find $[\omega_{\text{out}}]_m = \arg \min_{\omega \in \mathcal{V}} \|[\omega_{\text{in}}]_m - \omega\|^2$.
 - 3: **end for**
-

where $s \in \mathbb{C}$ represents an automatic normalization factor, which resolves the scaling issue of \mathbf{g} when designing the beam pattern [19].

To tackle the RIS configuration design problem in (4), we apply a projected gradient descent algorithm as described in Algorithm 1, inspired by [19, Alg. 2]. First, the technique performs one gradient decent step w.r.t. the scaling variable s in Line 2 of Algorithm 1. Next, an unconstrained gradient decent step is performed w.r.t. the RIS configuration in Line 3, and the result is projected onto set \mathcal{V} in Line 4 to satisfy the look-up table constraint in (4b). Here, β is a design parameter that controls the step size and $\lambda_{\max}(\cdot)$ denotes the largest eigenvalue of the matrix argument. The projection step is described in Algorithm 2.

B. Proposed Reduced-Complexity Solution

Since $G(\mathbf{p})$ is defined over a 3D domain, N_G becomes very large, leading to a high complexity requirement for Algorithm 1. To avoid this complexity, we propose to express the complex beam pattern in spherical coordinates and re-define our objective function in (4). In the case of far-field communications, $G(\mathbf{p})$ can be expressed as $G(\theta, \phi)$, where θ is the azimuth angle and ϕ is the elevation angle, defined with respect to the RIS coordinates system (see Fig. 1), similar to the approach in [26, Fig.1b].

Furthermore, for the case of multiple concurrent beams, we choose to cover $I \geq 1$ reference RX positions $\mathbf{p}_{\text{ref},i}$'s, with $i = 1, 2, \dots, I$, each with spherical coordinates $[\rho_{\text{ref},i}, \theta_{\text{ref},i}, \phi_{\text{ref},i}]^T$, aiming at precise beam approximation. The latter preference positions are defined as:

$$\mathbf{g}_{\rho,i} = G([\rho, \theta_{\text{ref},i}, \phi_{\text{ref},i}]^T), \quad \rho \in \mathcal{R}, \quad (5)$$

$$\mathbf{g}_{\theta,i} = G([\rho_{\text{ref},i}, \theta, \phi_{\text{ref},i}]^T), \quad \theta \in \mathcal{T}, \quad (6)$$

$$\mathbf{g}_{\phi,i} = G([\rho_{\text{ref},i}, \theta_{\text{ref},i}, \phi] ^T), \quad \phi \in \mathcal{P}, \quad (7)$$

where \mathcal{R} , \mathcal{T} , and \mathcal{P} are discretization sets of the three spherical coordinates ρ , θ , and ϕ . Similarly, we define the corresponding RIS response vectors, e.g., for the azimuth angle: $\mathbf{B}_{\theta,i} = [\mathbf{b}_{\theta,i,1}^T; \dots; \mathbf{b}_{\theta,i,|\mathcal{T}|}^T]$ where $\mathbf{b}_{\theta,i,k}^T = \mathbf{b}([\rho_{\text{ref},i}, \theta_k, \phi_{\text{ref},i}]^T)$ for θ_k being the k -th element ($k = 1, 2, \dots, |\mathcal{T}|$) in \mathcal{T} . Putting all

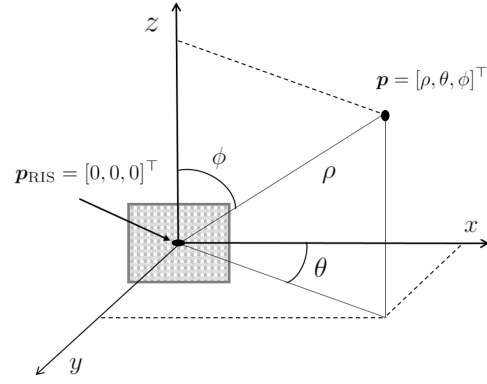


Fig. 1: The geometry with respect to the RX point \mathbf{p} , where the RIS center is point \mathbf{p}_{RIS} that serves as the origin of both the spherical and Cartesian coordinates systems.

Algorithm 3 Reduced-Complexity RIS Configuration Design

Initialize: $\beta \in (0, 1)$, $\omega^{(0)} = \text{proj}_{\mathcal{V}}(\sum_{i=1}^I \sum_{\mathbf{p} \in \{\rho, \theta, \phi\}} \mathbf{B}_{\mathbf{p},i}^\dagger \mathbf{g}_{\mathbf{p},i})$.

- 1: **for** $r = 1, 2, \dots$ **do**
- 2: Update the scaling factor as:

$$s^{(r)} = \sum_{i=1}^I \sum_{\mathbf{p} \in \{\rho, \theta, \phi\}} \frac{(\omega^{(r-1)})^H \mathbf{B}_{\mathbf{p},i}^H \mathbf{g}_{\mathbf{p},i}}{\|\mathbf{B}_{\mathbf{p},i} \omega^{(r-1)}\|^2}. \quad (9)$$

- 3: Update the RIS configuration as:

$$\omega_u^{(r)} = \omega^{(r-1)} + \quad (10)$$

$$\beta \sum_{i=1}^I \sum_{\mathbf{p} \in \{\rho, \theta, \phi\}} \frac{(s^{(r)})^* \mathbf{B}_{\mathbf{p},i}^H (\mathbf{g}_{\mathbf{p},i} - s^{(r)} \mathbf{B}_{\mathbf{p},i} \omega^{(r-1)})}{\lambda_{\max}(|s^{(r)}|^2 \mathbf{B}_{\mathbf{p},i}^H \mathbf{B}_{\mathbf{p},i})}$$

- 4: Perform the projection: $\omega^{(r)} = \text{proj}_{\mathcal{V}}(\omega_u^{(r)})$.
 - 5: **end for**
-

above together, we formulate the following new optimization problem:

$$\min_{s, \omega} \sum_{i=1}^I \sum_{\mathbf{p} \in \{\rho, \theta, \phi\}} \|\mathbf{g}_{\mathbf{p},i} - s \mathbf{B}_{\mathbf{p},i} \omega\|^2 \quad (8a)$$

$$\text{s.t. } \omega_m \in \mathcal{V}, m = 1, \dots, M. \quad (8b)$$

We note that $|\mathcal{R}| + |\mathcal{T}| + |\mathcal{P}| \ll |\mathcal{R}| \times |\mathcal{T}| \times |\mathcal{P}| = N_G$. The algorithm for solving (8) is summarized in Algorithm 3.

IV. NUMERICAL RESULTS

In this section, we present various numerical results for the proposed RIS-based beam pattern approximation approach.

A. Simulation Parameters

In our investigations for the proposed beam pattern design approach, we have considered realistic lookup tables characterizing the experimental complex responses per unit element (i.e., the set of values for the reflection coefficient per element) of two distinct RIS hardware prototypes, which have been recently developed in the framework of the EU H2020 RISE-

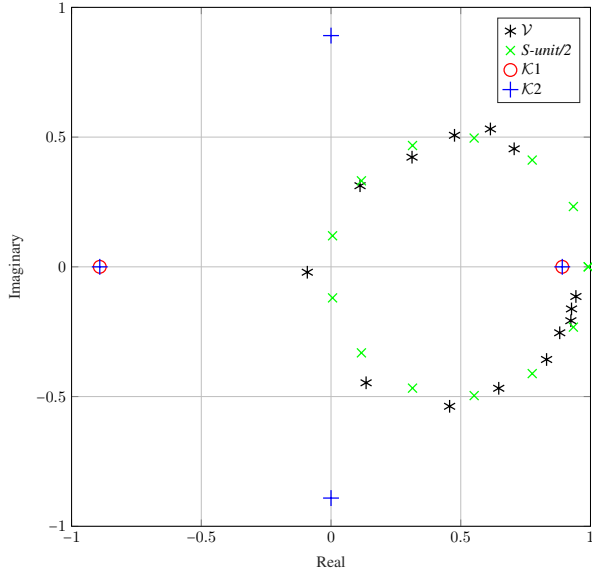


Fig. 2: The sets \mathcal{V} , $\mathcal{K}1$, and $\mathcal{K}2$ with the values for the RIS elements responses, as well as a downscale-shifted unit-modulus set, plotted in the complex plane.

6G² project. In particular, the following sets with RIS elements responses were considered:

- A set \mathcal{V} from [21, Table 1] including 14 different values for the reflection state of each RIS element.
- A set $\mathcal{K}1$ from [20] with 2 different values per RIS element.
- A set $\mathcal{K}2$ resulting from the modification of the single-diode varactor approach in [20] with 1-bit quantization at each RIS element, based on p-i-n diodes with 2-bit quantization.

The distribution of the reflection coefficients of the considered three sets in the complex plane is shown in Fig. 2. As observed, the set \mathcal{V} can be approximated by the scaled and shifted unit circle $\omega_m = 0.5(1 + e^{j\psi}) \forall m = 1, 2, \dots, M$, with $\psi \in [0, 2\pi)$, which is represented in the figure by the $S\text{-unit}/2$.

As for other simulation parameters, we have considered the carrier frequency 5.15 GHz with set \mathcal{V} , as well as the 28 GHz frequency with sets $\mathcal{K}1$ and $\mathcal{K}2$, in order to reflect the actual operating frequency of each RIS hardware prototype. In addition, we have set $\mathbf{p}_{\text{des},1} = [2, 3, 2]$ m for both directional and derivative beam patterns (i.e., with $I = 1$), whereas $\mathbf{p}_{\text{des},1} = [0, 4, 2]$ m and $\mathbf{p}_{\text{des},2} = [0, 4, 4]$ m were considered for the double-beam pattern (i.e., with $J = I = 2$). Finally, we used $\mathbf{p}_{\text{TX}} = [5, 5, 0]$ m and placed the RIS as $\mathbf{p}_{\text{RIS}} = [0, 0, 0]$ m, having in total $M = 32 \times 32$ elements.

B. Results and Discussion

We hereinafter evaluate the designed beams in both 1D and 2D. The 1D visualizations show the performance of the considered beam design methods, allowing us to evaluate the designed beams in the intended directions, whereas the 2D illustrations showcase the beam pattern in terms of both the

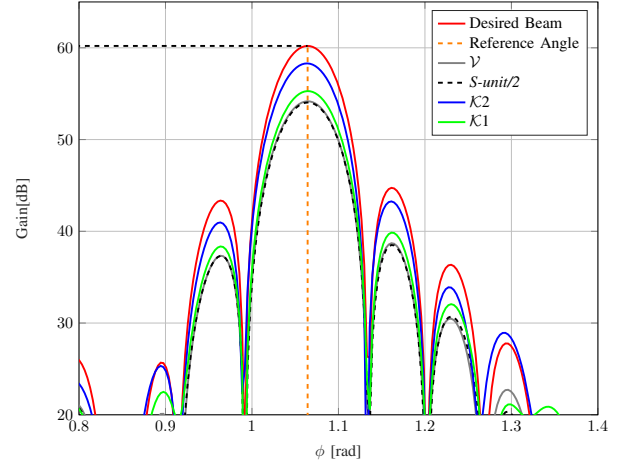


Fig. 3: Directional beam patterns as a function of the elevation angle ϕ for various beam synthesis methods under gradual RIS hardware constraints, including the realistic RIS element responses of [20], [21].

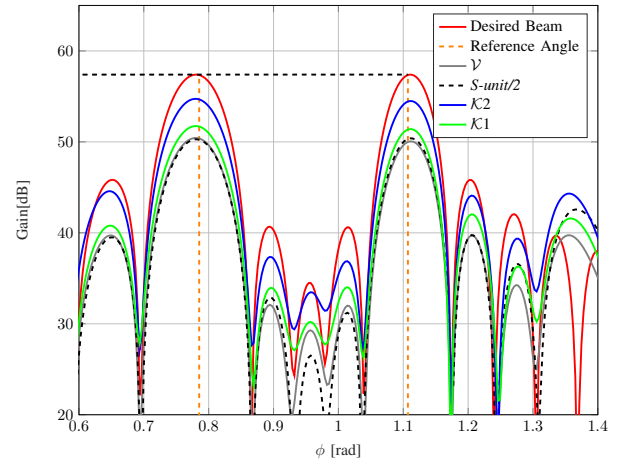


Fig. 4: Two-peak beam patterns as a function of the elevation angle ϕ for various beam synthesis methods under gradual RIS hardware constraints, including the realistic RIS element responses of [20], [21].

azimuth and elevation angles. All visualizations include the magnitude $|G(\mathbf{p})|$ in 1D or 2D slices in spherical coordinates.

1) *1D Visualization*: In Figs. 3–5, we show respectively the optimized 1D directional, multi-beam, and derivative patterns as a function of ϕ , while setting the two other coordinates to their true reference values. These patterns have been generated without any constraint on the controlled RIS precoder (*desired*), with a unit-modulus constraint (*unit*), a downscale-shifted unit-modulus constraint (*S-unit/2*), and finally with realistic constraints from lookup tables (corresponding to sets \mathcal{V} , $\mathcal{K}1$, and $\mathcal{K}2$). Note that the downscale-shifted unit-modulus constraint is introduced as a benchmark for the set \mathcal{V} , keeping the same number of discrete complex values (i.e., equal to 14).

In Fig. 3, we first remark that the desired directional beam (red curve) has a peak of 60.2 dB, which is aligned with the beamforming gain offered by the considered $M = 1024$ RIS elements. As expected, the beam projection onto $S\text{-unit}/2$

²See <https://RISE-6G.eu> for more information.

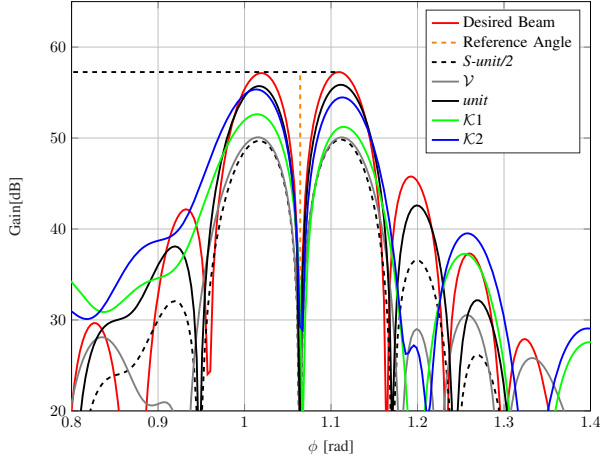


Fig. 5: Derivative beam patterns as a function of the elevation angle ϕ for various beam synthesis methods under gradual RIS hardware constraints, including the realistic RIS element responses of [20], [21].

(black curve) shows a loss of about 6 dB, as $\|\omega\|^2$ is divided by a factor of 4, whereas the *unit* beam (not shown here) is obviously the same as the *desired* one (e.g., using a steering vector). When comparing *S-unit/2* with the set \mathcal{V} (gray curve), we notice a very similar performance and peak value resulting from the fact that the elements of \mathcal{V} are positioned close to those of the scaled and shifted unit circle (refer to Fig. 2). Furthermore, while comparing the beam projected on the set $\mathcal{K}1$ (i.e., with 1-bit unit cells; green curve) with the desired beam, we also observe a significant loss, which is however mitigated by about 3 dB, when constraining the beam onto the set $\mathcal{K}2$ (i.e., with 2-bit unit cells; blue curve).

The double-beam case is illustrated in Fig. 4. As expected, in comparison with the *desired* directional beam pattern, a 3 dB loss exists at the two beam peaks of the optimized multi-beam pattern, which aims at serving 2 distinct desired RX positions in the coverage area. It is also noted that, for both derivative and multi-beam patterns, the same general trends as that for the directional beam pattern are observed, as a function of the different RIS hardware constraints. Finally, in the derivative beam in Fig. 5, we see the presence of a null when ϕ corresponds to the true desired position, as already pointed out in [14]. It is also evident from the figure that the sets $\mathcal{K}1$ and $\mathcal{K}2$ have difficulties to follow the rapid variations of the desired beam, leading to severe side lobes. This happens due to the small number of quantization levels.

2) *2D Visualization*: The heatmaps in Fig. 6 show, as a function of the direction of departure from the RIS and for a given desired direction (red circle), the *desired* directional beam, as well as the same beam projected onto sets $\mathcal{K}1$, $\mathcal{K}2$, and \mathcal{V} , respectively. In Fig. 6a, we observe that for the directional beam, the main beam is present in the desired direction, as expected. Note that this setting is just used as a baseline reference for further comparisons with the optimized beams obtained under pragmatic RIS hardware constraints.

In Fig. 6b, using the set $\mathcal{K}1$, a beam is still observed

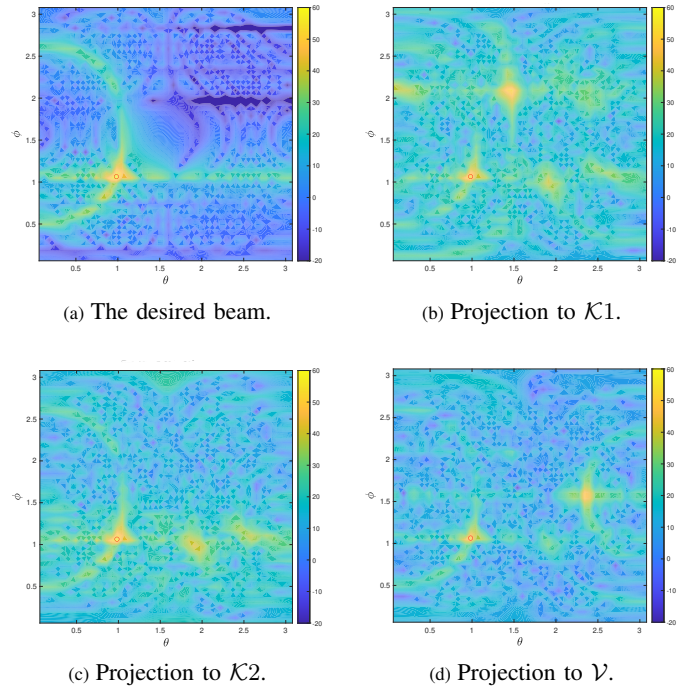


Fig. 6: Illustration of a directional beam pattern pointing to one single desired direction (red circle), as a function of angles ϕ (elevation) and θ (azimuth).

in the desired direction, even though clearly attenuated in comparison with the *desired* beam from Fig. 6a. We also note the presence of a strong and systematic secondary grating lobe, which turns out to be a standard reflection, whose direction is symmetric to the direction of arrival of the impinging wave, regardless of the desired beam direction, number of RIS elements, or inter-elements spacing. This kind of grating lobe arises due to the severe quantization of the RIS element phase, creating some kind of spatial aliasing. However, as shown on Fig. 6c, this problem of grating lobe can be solved after adding only one more bit of phase quantization. In this case, a higher peak value (by about +3 dB) is also achieved for the main lobe in the desired direction, even if the levels of all the other secondary lobes remain globally high and comparable to those in the 1-bit phase quantization case.

Finally, Fig. 6d depicts the beam pattern result using \mathcal{V} . Despite the large number of quantization levels (specifically, 14 levels), a grating lobe is still present; in this case, this appears towards a fixed direction. Now the grating lobe is due to the set \mathcal{V} not being centered at the origin. Beyond this specular grating lobe, the levels of all the secondary lobes are also clearly increased on average over the entire 2D domain.

V. CONCLUSION AND FUTURE WORK

In this paper, we introduced a generic low-complexity method for optimizing the complex profile of reflective RISs so as to generate arbitrary beam patterns under realistic RIS hardware constraints. The proposed method makes use of a pre-characterized lookup table containing feasible RIS element-wise reflection coefficients. Concrete illustrations of

directional, multi-beam, and derivative beam patterns have been provided in a canonical validation case, while considering gradual hardware constraints (including that of real RIS prototypes currently under development). Overall, our first observations stress out the dominating impact of both the phase quantization levels and the power loss (and accordingly, the span of practically valid phases) of the element-wise reflection coefficients, with respect to the beam peak power generated in the desired RX direction(s) and to the presence of harmful undesired lobes.

Future works should investigate the practical performance of RIS-empowered multi-user communications, localization, and sensing at system level, while applying the proposed method under realistic hardware constraints (rather than restricting the study to beam patterns only), as well as the design of new RIS hardware prototypes offering even more suitable feasible complex sets, whose distribution in the complex plane shall typically be centered and as close as possible to the unit circle. Moreover, a more in-depth quantitative analysis and comparison with the least-squares beamforming algorithm of [19] needs to be performed.

ACKNOWLEDGMENT

This work has been supported, in part, by the EU H2020 RISE-6G project under grant 101017011 and by the MSCA-IF grant 888913 (OTFS-RADCOM).

REFERENCES

- [1] C. Huang, A. Zappone, G. C. Alexandropoulos, M. Debbah, and C. Yuen, "Reconfigurable intelligent surfaces for energy efficiency in wireless communication," *IEEE Trans. Wireless Commun.*, vol. 18, pp. 4157–4170, Aug. 2019.
- [2] Q. Wu and R. Zhang, "Intelligent reflecting surface enhanced wireless network via joint active and passive beamforming," *IEEE Trans. Wireless Commun.*, vol. 18, pp. 5394–5409, Nov. 2019.
- [3] E. Calvanese Strinati, G. C. Alexandropoulos, H. Wymeersch, B. Denis, V. Sciancalepore, R. D'Errico, A. Clemente, D.-T. Phan-Huy, E. D. Carvalho, and P. Popovski, "Reconfigurable, intelligent, and sustainable wireless environments for 6G smart connectivity," *IEEE Commun. Mag.*, vol. 59, pp. 99–105, Oct. 2021.
- [4] E. Calvanese Strinati, G. C. Alexandropoulos, V. Sciancalepore, M. Di Renzo, H. Wymeersch, D.-T. Phan-Huy, M. Crozzoli, R. D'Errico, E. D. Carvalho, P. Popovski, P. D. Lorenzo, L. Bastianelli, M. Belouar, J. E. Mascolo, G. Gradoni, S. Phang, G. Lerosey, and B. Denis, "Wireless environment as a service enabled by reconfigurable intelligent surfaces: The RISE-6G perspective," in *Proc. Joint EuCNC & 6G Summit*, (Porto, Portugal), Jun. 2021.
- [5] C. Huang, S. Hu, G. C. Alexandropoulos, A. Zappone, C. Yuen, R. Zhang, M. Di Renzo, and M. Debbah, "Holographic MIMO surfaces for 6G wireless networks: Opportunities, challenges, and trends," *IEEE Wirel. Commun.*, vol. 27, no. 5, pp. 118–125, Oct. 2020.
- [6] S. Hu, F. Rusek, and O. Edfors, "Capacity degradation with modeling hardware impairment in large intelligent surface," in *Proc. IEEE GLOBECOM*, (Abu Dhabi, UAE), Dec. 2018.
- [7] H. Shen, W. Xu, S. Gong, C. Zhao, and D. W. K. Ng, "Beamforming optimization for IRS-aided communications with transceiver hardware impairments," *IEEE Trans. Commun.*, vol. 69, pp. 1214–1227, Feb. 2020.
- [8] A. F. Molisch, V. V. Ratnam, S. Han, Z. Li, S. L. H. Nguyen, L. Li, and K. Haneda, "Hybrid beamforming for massive MIMO: A survey," *IEEE Commun. Mag.*, vol. 55, pp. 134–141, Sept. 2017.
- [9] G. C. Alexandropoulos, N. Shlezinger, and P. del Hougne, "Reconfigurable intelligent surfaces for rich scattering wireless communications: Recent experiments, challenges, and opportunities," *IEEE Commun. Mag.*, vol. 59, pp. 28–34, Jun. 2021.
- [10] S. Abeywickrama, R. Zhang, Q. Wu, and C. Yue, "Intelligent reflecting surface: Practical phase shift model and beamforming optimization," *IEEE Trans. Commun.*, vol. 68, pp. 5849–5863, Sep. 2020.
- [11] R. Long, Y.-C. Liang, Y. Pei, and E. G. Larsson, "Active reconfigurable intelligent surface-aided wireless communications," *IEEE Trans. Wireless Commun.*, vol. 20, pp. 4962–4975, Aug. 2021.
- [12] C. Huang, G. C. Alexandropoulos, A. Zappone, M. Debbah, and C. Yuen, "Energy efficient multi-user MISO communication using low resolution large intelligent surfaces," in *Proc. IEEE GLOBECOM*, (Abu Dhabi, UAE), Dec. 2018.
- [13] J. A. Zhang, X. Huang, Y. J. Guo, J. Yuan, and R. W. Heath Jr., "Multibeam for joint communication and radar sensing using steerable analog antenna arrays," *IEEE Trans. Veh. Technol.*, vol. 68, pp. 671–685, Jan. 2019.
- [14] F. Keskin, F. Jiang, F. Munier, G. Seco-Granados, and H. Wymeersch, "Optimal spatial signal design for mmwave positioning under imperfect synchronization," *IEEE Trans. Veh. Technol.*, to appear, 2022.
- [15] U. Nickel, "Overview of generalized monopulse estimation," *IEEE Trans. Aerosp. Electron. Syst.*, vol. 21, pp. 27–56, Jun. 2006.
- [16] M. Rahal, B. Denis, K. Keykhosravi, B. Uguen, and H. Wymeersch, "RIS-enabled localization continuity under near-field conditions," in *Proc. IEEE SPAWC*, (Lucca, Italy), 2021.
- [17] A. Agrawal and E. Holzman, "Beamformer architectures for active phased-array radar antennas," *IEEE Trans. Antennas Prop.*, vol. 47, pp. 432–442, Mar. 1999.
- [18] S. H. Talisa, K. W. O'Haver, T. M. Comberiate, M. D. Sharp, and O. F. Somerlock, "Benefits of digital phased array radars," *Proc. IEEE*, vol. 104, pp. 530–543, Mar. 2016.
- [19] J. Tranter, N. D. Sidiropoulos, X. Fu, and A. Swami, "Fast unit-modulus least squares with applications in beamforming," *IEEE Trans. Signal Process.*, vol. 65, pp. 2875–2887, Jun. 2017.
- [20] L. Di Palma, A. Clemente, L. Dussopt, R. Sauleau, P. Potier, and P. Pouliguen, "Circularly-polarized reconfigurable transmitarray in K-band with beam scanning and polarization switching capabilities," *IEEE Trans. Antennas Prop.*, vol. 65, pp. 529–540, Feb. 2017.
- [21] R. Fara, P. Ratajczak, D.-T. P. Huy, A. Ourir, M. Di Renzo, and J. De Rosny, "A prototype of reconfigurable intelligent surface with continuous control of the reflection phase," *arXiv:2105.11862*, 2021.
- [22] E. Basar, M. Di Renzo, J. De Rosny, M. Debbah, M.-S. Alouini, and R. Zhang, "Wireless communications through reconfigurable intelligent surfaces," *IEEE access*, vol. 7, pp. 116753–116773, 2019.
- [23] Z. Abu-Shaban, K. Keykhosravi, M. F. Keskin, G. C. Alexandropoulos, G. Seco-Granados, and H. Wymeersch, "Near-field localization with a reconfigurable intelligent surface acting as lens," in *Proc. IEEE ICC*, (Montreal, Canada), Jun. 2021.
- [24] A. Kakkavas, G. Seco-Granados, H. Wymeersch, M. H. C. Garcia, R. A. Stirling-Gallacher, and J. A. Nossek, "5G downlink multi-beam signal design for LOS positioning," in *Proc. IEEE GLOBECOM*, (Madrid, Spain), 2019.
- [25] J. Li, L. Xu, P. Stoica, K. W. Forsythe, and D. W. Bliss, "Range compression and waveform optimization for MIMO radar: A Cramér-Rao bound based study," *IEEE Trans. Signal Process.*, vol. 56, pp. 218–232, Jan. 2008.
- [26] K. Keykhosravi, M. F. Keskin, G. Seco-Granados, and H. Wymeersch, "SISO RIS-enabled joint 3D downlink localization and synchronization," in *Proc. IEEE ICC*, (Montreal, Canada), 2021.